FULL PAPER

Crystal Size, Morphology, and Growth Mechanism in Bio-Inspired Apatite Nanocrystals

José Manuel Delgado-López, Ruggero Frison, Antonio Cervellino, Jaime Gómez-Morales, Antonietta Guagliardi,* and Norberto Masciocchi

Bio-inspired apatite nanoparticles precipitated in the presence of citrate ions at increasing maturation times are characterized in terms of structure, size, morphology, and composition through advanced X-ray total scattering techniques. The origin of the platy crystal morphology, breaking the hexagonal symmetry, and the role of citrate ions is explored. By cross-coupling the size and shape information of crystal domains with those obtained by atomic force microscopy on multidomain nanoparticles, a plausible mechanism underlying the amorphous-to-crystal transformation is reconstructed. In the present study, citrate plays the distinct roles of inducing the platy morphology of the amorphous precursor and controlling the thickness of the Ca-deficient apatite nanocrystals. These findings can open new scenarios also in bone mineralization, where citrate might have a broader role to play than has been thought to date.

1. Introduction

Biomimetic apatite nanoparticles (NPs) are very similar in size, shape and composition to the mineral component of bone and teeth. They are extensively investigated and used either as system models, to explore fundamental aspects of knotty mineralization phenomena, or as multifunctional materials, to aid a number of biomedical applications (from regenerative medicine and bone tissue engineering to drug delivery).[1] Bone is an organic–inorganic composite in which carbonated apatite nanocrystals (NCs) grow through a complex biomineralization process from an amorphous calcium phosphate (ACP) precursor. Control over crystal morphology is thought be regulated mainly through interaction with collagen fibrils and some

acidic non-collagenous proteins,[2] ending up with tiny crystal platelets. The platy shape of the mineral plays an important role in determining the unique functional properties of bone[3] and is a key structural feature to be controlled in biomimetic apatites. However, platelets do not develop normal to the crystallographic c-axis of the hexagonal apatite crystal structure (space group $P6_3/m$),[4] therefore breaking the crystal symmetry through a mechanism that, so far, has remained unclear. Whether or not such morphology is reminiscent of an unstable transient precursor (amorphous and/or intermediate, such as the octacalcium phosphate)[5] is still a matter of debate.

The scenario of living organisms secreting mineralized tissues counts many cases of a transient amorphous precursor determining the final crystal morphology.[6] ACP is highly unstable and the mechanism underlying the ACP-to-apatite transformation and clarifying the origin of platy crystals has never been directly detected, neither in in vivo nor in vitro experiments. Moreover, spherical ACP particles are reported at the early stages of the precipitation process and apatite platelets are observed as the final crystalline product.[2b,7] In this view, the role of small molecules, such as citrate, has traditionally been neglected. Organic, low-molecular-weight additives are frequently used nowadays in the synthesis of biomimetic apatites to control the crystal growth within the nanometer regime.[8] Among these, citrate molecules might play a broader role than a simple synthetic additive and directly intervene in bone mineralization. Indeed, solid-state NMR studies have recently put in evidence the relatively large amount of citrate in bone, where it accounts for about 5.5 wt% of the total organic component, and assessed the role of this small molecule in stabilizing the size and morphology of bone apatite.[9] According to Schmidt-Rohr and co-workers,[9a] the distance of carboxylate groups in citrate matches that of pairs of neighboring Ca^{2+} ions at the $(10\bar{1}0)$ facets of the apatite crystal, causes citrate to be strongly bound to the apatite facets and blocks growth along this direction, thus limiting the platelet thickness. To support this hypothesis, Xie and Nancollas[9b] outlined the differences between bone and tooth enamel: the much lower content of citrate in saliva and the mismatch of carboxylate groups at the crystal surface of fluoro-apatite turn into a rod-like crystal morphology. However, how, and to what extent, citrate ions influence nucleation and crystal growth in the absence of other organic constituents is difficult

Dr. J. M. Delgado-López, Dr. J. Gómez-Morales
Laboratorio de Estudios Cristalográficos
IACT (CSIC-UGR), Avda. de las Palmeras
4, E-18100 Armilla, Granada, Spain
Dr. R. Frison, Dr. A. Guagliardi
Istituto di Cristallografia,
CNR, and To.Sca.Lab. via Lucini 3, I-22100, Como, Italy
E-mail: antonella.guagliardi@ic.cnr.it
Dr. A. Cervellino
Swiss Light Source
Paul Scherrer Institut
CH-5232, Villigen, Switzerland
Prof. N. Masciocchi
Dipartimento di Scienza e Alta Tecnologia and To.Sca.Lab.
Università dell'Insubria
Via Valleggio 11, I-22100, Como, Italy

Materials
Views
www.MaterialsViews.com

ADVANCED
FUNCTIONAL
MATERIALS
www.afm-journal.de

FULL PAPER

to disentangle in biological systems and only rarely explored in synthetic models.[10]

Herein, we used citrate-bio-inspired apatite NPs as the system model. Samples were prepared at 80 °C (to access to crystal maturation process on a reasonable timescale), collected at increasing precipitation times and investigated by advanced X-ray total scattering modeling[11] and atomic force microscopy (AFM). The presence of citrate molecules provided two distinct advantages in this study: 1) slowing down the transformation of ACP-to-apatite, which enabled us to take "snapshots" of the nanocrystal structural and morphological changes in time; 2) focusing on the sole role of citrate in controlling the crystal properties. Indeed, in vitro, citrate ions are not expected to drive, alone, the crystal morphology to platelets, as the reported distance-matching criterion would apply in the same manner to all six, symmetry equivalent, $\{01\bar{1}0\}$ facets of the hexagonal apatite structure.[12]

Wide-angle X-ray and neutron scattering have traditionally been used to investigate the apatite crystal structure; much less is known about the great potential of Total Scattering methods to provide a quantitative approach for studying, at the atomic and nanometer length scales, both the structure and the shape of apatite NCs. Indeed, these methods offer the unique advantage, compared to conventional diffraction, of treating Bragg and diffuse scattering (originating from long-range order and short-range effects, respectively) on an equal footing.[13] They are developed both in direct (radial or pair distribution function)[11a] and reciprocal space (Debye equation).[11b] The first approach provides a 1D plot of density peaks at atomic separations, the second one makes use of interatomic distances derived from model NPs to reproduce the experimental pattern. Here, Total Scattering techniques have been the method of choice to quantitatively characterize nanosized and disordered bio-inspired apatite NCs in terms of structure, composition, size and morphology. Moreover, by cross-coupling the size and shape information of crystal domains with those obtained by AFM on multidomain NPs, we reconstructed ex situ the amorphous-to-crystal transformation process at molecular scale resolution and proposed a plausible mechanism inducing the platy morphology of crystals.

The paper is organized as follows: Section 2 deals with the total scattering characterization of the bio-inspired apatite nanoparticles and the modeling details; Section 3 is dedicated to the AFM study of the investigated samples; in Section 4, the extended discussion of the main results is presented, leading to the mechanistic description of apatite growth process.

2. Total Scattering Characterization of Bio-Inspired Apatite Nanoparticles

In order to study the structural, compositional, and morphological evolution of apatite nanocrystals in the system model, we investigated samples precipitated at 5 min, 4 h, and 96 h, either in the presence (cAp samples) or in the absence (Ap samples) of sodium carbonate, CO_3^{2-} being the major phosphate substituent in biological apatites.[14] The Debye function analysis (DFA) method was here applied to characterize biomimetic apatites taking care, for the first time, of all the experimental
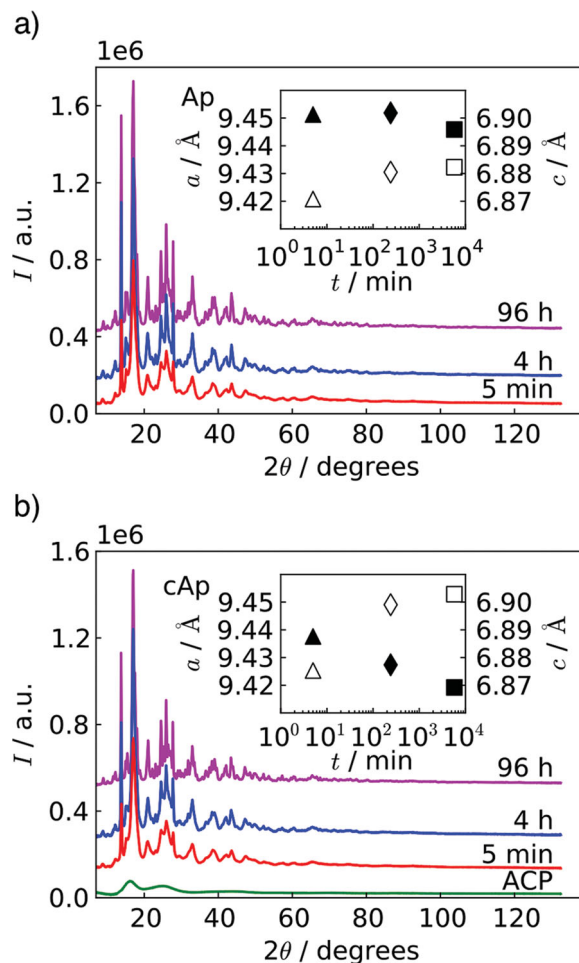

Figure 1. Synchrotron diffraction data of Ap (a) and cAp (b) samples at different maturation times (5 min, 4 h, 96 h, vertically offset for the sake of clarity) collected with a wavelenght of 0.82699 Å. The ACP sample is instantaneously precipitated (cAp conditions) and shows the typical pattern features of an amorphous material. Insets: effects of the CO_3^{2-}/PO_4^{3-} substitution on the lattice parameters; the contraction of the a-axis (filled symbols: ▲5 min; ◆4 h; ■96 h) and the expansion of the c-axis (empty symbols: △5 min; ◇4 h; □96 h) are rather limited in Ap samples and more pronounced in cAp ones.

requirements (angle-dependent intensity correction for absorption effects and subtraction of extra-sample scattering contributions, see the Experimental Section) and enabling a modeling approach free of any phenomenological component. **Figure 1** shows the synchrotron X-ray scattering data of all citrate-controlled samples after these corrections. The Ap and cAp datasets in Figure 1 were processed by the DFA method described in section 2.1. A sample instantaneously precipitated in the presence of sodium carbonate was also analyzed; its diffraction pattern (ACP in Figure 1b) shows the typical features of an amorphous calcium phosphate and was further characterized through the radial distribution function method, as described in Section 2.2. Noteworthy, in the absence of citrate ions (blank runs, briefly described in the Experimental Section) the reaction proceeds along a different pathway, initially leading to the precipitation of octacalcium phosphate; although highly interesting, this finding requires to be deeply investigated

through a dedicated study, which falls beyond the scope of this work.

2.1. Modeling Biomimetic Apatites through the Debye Equation

The total scattering method here used to characterize the apatite nanocrystals is based on a new and fast implementation of the Debye scattering equation. Debye's formula is known since 1915 and takes the advantage of simultaneously modeling Bragg and diffuse scattering as a function of the distribution of interatomic distances within the sample, as follows:

$$I(Q) = \sum_{j=1}^{N} f_j(Q)^2 \, o_j^2 + 2 \sum_{j>i=1}^{N} f_j(Q) f_i(Q) T_j(Q) T_i(Q) o_j o_i \frac{\sin(Qd_{ij})}{Qd_{ij}}$$

(1)

where $Q = 2\pi q$, $q = 2\sin\theta/\lambda$ is the length of the reciprocal scattering vector, λ is the radiation wavelength, f_j is the atomic form factor, d_{ij} is the interatomic distance between atoms i and j, N is the number of atoms in the nanoparticle. In this formula, thermal vibrations (or static disorder) and partial site occupancy factors are also taken into account by two atomic, adjustable parameters (T and o). The first summation addresses the contribution of the (zero) distances of each atom from itself, the second summation that of the non-zero distances between pairs of distinct atoms. In its original formulation, the Debye equation is extremely expensive from the computational point of view, as the number of distinct interatomic distances increases with the nanoparticle linear size by a power law with exponent 2 and 6 for ordered and fully disordered materials, respectively (intermediate values apply to partially ordered cases). An original approach (here applied) was developed by some of us,[15] which makes use of *sampled* interatomic distances instead of the original ones, and reduces the number of terms in the Debye equation by orders of magnitude (growing just as the *linear* NC dimension), without losing accuracy in the pattern calculation. Furthermore, the constant step used for encoding the sampled distances and the recursive properties of Chebyshev polynomials of the second kind made the calculations fast enough to deal with the pattern of hundreds of nanocrystals and to use iterative global optimization algorithms.

The DFA modeling strategy here applied, can be summarized in the following steps: *i)* A bottom-up approach was used to generate a population of atomistic nanocrystal models of increasing size, using the crystal unit cell of a Ca-deficient hydroxyapatite[16] (CDHA) as the building block. Hexagonal prisms (**Figure 2**a) were built through a layer-by-layer construction and under the assumption of two independent "growth" directions, one along the six-fold symmetry *c* axis and the second one in the orthogonal *ab* plane, up to 15 nm in *ab* and 50 nm along *c*. *ii)* The sampled interatomic distances of each nanocrystal were computed and stored in suitable databases to be used in the subsequent DFA process. *iii)* To best match the experimental traces, a number of adjustable parameters were involved in the pattern model. To account for (number- and mass-based) size and shape distributions of the bivariate population of CDHA nanocrystals, we adopted a bivariate log-normal function[17] with five adjustable parameters (the average/standard deviation pairs of the size
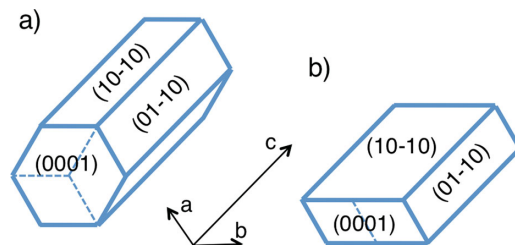

Figure 2. a) Hexagonal and b) platy morphologies of Ca-deficient hydroxyapatite crystals used in the DFA modeling; the platy morphology comes from an independent growth along *a*- and *b*-axes therefore breaking the hexagonal crystal symmetry. *(h, k, -h-k, l)* indices of the most relevant crystal facets are provided.

distributions along the two growth directions and their correlation angle). Among the structural parameters, we refined the atomic site occupancy factors of the two Ca and the hydroxyl O atoms (see inset of **Figure 3**) and all the isotropic atomic Debye–Waller factors (the phosphate O atoms were constrained to the same value, to limit the number of parameters). *iv)* In order to deal with the platy CDHA shapes discussed in section 1, *bivariate* populations of crystals grown along *c*, and, in *ab*, by considering anisotropic, parallelogram-shaped bases with fixed 1:2 *a:b* ratio (Figure 2b), were built. These populations were used *together* with the hexagonal base prisms defined in *i)* and constrained to the same NC size distribution and stoichiometry values, in a *biphasic* pattern model. When both the hexagonal and platy morphologies were used, the Goodness of fit (see Experimental Section) obtained by matching the experimental and the model patterns were systematically better than the model relying on the hexagonally shaped apatite only. A platy shape population based on a fixed 1:3 *a:b* ratio was also tested: it provided worse (5 min samples) or comparable (4 h and 96 h samples) Gof's than the 1:2 *a:b* ratio case, which was therefore adopted to describe the platy morphology in all samples.
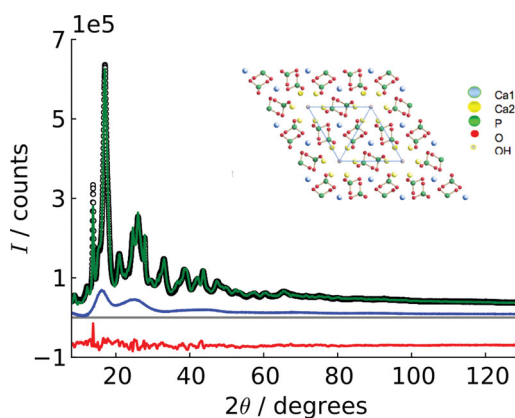

Figure 3. Best fit of the cAp 5 min sample provided by the DFA method: experimental powder diffraction pattern (empty circles); total model pattern (green line) with its amorphous component (blue line); residual between experimental and model patterns (red line, shifted downwards for the sake of clarity). Agreement indices: GoF = 5.34, R_{wp} = 3.80. Inset: crystal structure of hydroxyapatite, viewed down [001]. Ca2 atoms design the so-called ion-channels, which elongates parallel to the crystallographic *c*-axis, where OH⁻ ions are located.

Materials
Views
www.MaterialsViews.com

ADVANCED
FUNCTIONAL
MATERIALS
www.afm-journal.de

FULL PAPER

The combination of hexagonal and platy shapes is a way to approximate, within our DFA approach, a trivariate size distribution, which in itself is too complex to be extracted from even high quality diffraction data. This approximation allowed the shape anisotropy of the *ab*-base (in addition to the anisotropy due to the crystal elongation in the *c*-axis direction) to be quantified without introducing too many unnecessary parameters. Such anisotropy can be measured by the ratio A of the base shape principal inertia moments (major/minor). In our model (1:2 *a:b* ratio), A = 1 for the hexagonal base, A = 6.17 for the platelet base. This measure is linear in the mass fraction, therefore an effective average base anisotropy <A> can be derived for the whole sample through the mass fractions of the two populations (normalized to the total crystalline component), differing only for the anisotropy of the *ab*-base shape. In the manuscript we directly referred to the mass fractions of the two morphologically distinct apatite populations for indicating the degree of anisotropy in the *ab*-plane instead of using the values of the <A> parameter, which are however reported for all samples in Table SI.2, Supporting Information.

Finally, the occurrence of an amorphous component was detected in all samples along with the nanosized apatites. This amorphous component was taken into account by using the experimental dataset of the ACP sample as a blank curve, scaled as part of the total pattern model by linear least squares (no additional background contributions were needed). Moreover, the integral area under the scaled ACP scattering trace was used to derive the ACP mass fraction in each sample (after normalization to electronic units and based on the chemical formula reported in the Experimental Section).

2.2. Structure, Composition, Size, and Morphology of Biomimetic Apatites

According to the DFA method described in Section 2.1, the synchrotron data of Ap and cAp samples were processed by considering two bivariate populations of Ca-deficient hydroxyapatite nanocrystals, having hexagonal[18] and platy shapes, respectively, and an additional amorphous phase modeled by suitably scaling the experimental ACP diffraction curve. The nano-sized apatites of the investigated samples mainly exhibited B-type carbonate substitutions[10c] (i.e., CO_3^{2-} replacing PO_4^{3-} into the apatite crystal lattice, as witnessed by FTIR spectroscopy) with CO_3^{2-}/PO_4^{3-} substitution in cAp samples (up to 8 wt% upon maturation) mimicking the biological case. The effects on cell parameters are shown in Figure 1 (insets) (see also Table SI.1, Supporting Information): a progressive unit cell *a*-axis contraction and a *c*-axis expansion are observed, that suggests an out-of-plane orientation of the vicariant carbonate anion (details are given in the Supporting Information, Figure SI.3). Maximum variations are rather limited in Ap (–0.06%, +0.17%) and more pronounced in cAp samples (–0.2% and +0.40%).

The best pattern model of the cAp 5 min sample is shown in Figure 3; plots of all the remaining samples are collected in Figure SI.1. For each dataset, the DFA provided relevant analytical, structural and microstructural information such as: i) the relative abundance of ACP and hexagonally/platy shaped CDHA; ii) the bivariate size distribution maps of CDHA
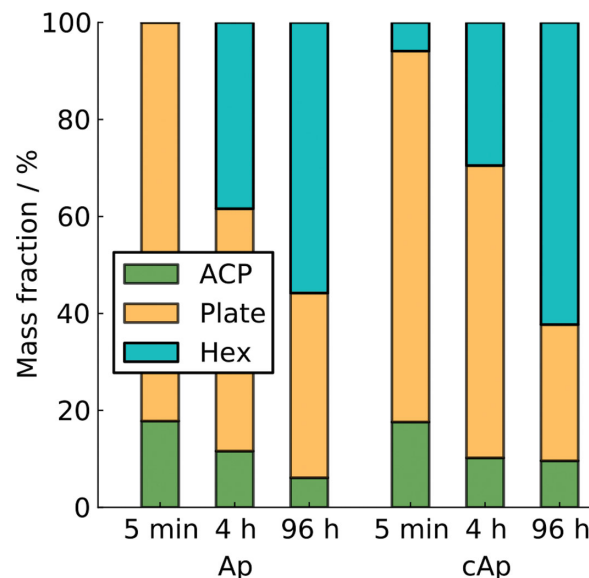

Figure 4. Relative abundance of amorphous (ACP) and crystalline (apatite) phases showing hexagonal or platy shape, as estimated by DFA for each Ap and cAp sample at growing maturation time.

nanocrystals and the average crystal size and shape derived there from; iii) the site occupancy factors of Ca and hydroxyl O atoms of the apatite structure (size-dependent in the largest crystals of samples precipitated at 96 h) and the Debye-Waller parameters of all atoms. **Figure 4** reports the variation of the weight percentage (wt%) of each of the three phases (ACP, hexagonal and platy apatites) in Ap and cAp samples at increasing maturation time (see also Table SI.2, Supporting Information). ACP is a minor component slowly decreasing upon maturation (from 17.8 to 6.1 wt% in Ap, from 17.6 to 9.6 wt% in cAp samples, respectively); nanocrystals of platy shape, varying from 82.2 to 38.1 wt% (Ap) and from 76.6 to 28.1 wt% (cAp), represent the total or nearly the total of the crystalline components at 5 min of maturation; they tend to decrease upon time, the hexagonally shaped ones becoming the major crystalline component after 96 h in both Ap (55.8 wt%) and cAp (62.3 wt%) samples.

As far as the DFA results on the crystal sizes, shapes, and their distributions are concerned, we show in **Figure 5**, as 2D maps, the refined (mass-based) bivariate size distributions of crystals obtained for a) cAp 5 min and b) cAp 96 h (similar maps are provided for the other samples in Figure SI.2, Supporting Information): the sizes are given as the diameter D_{ab} of the circle of equivalent area in the *ab*-plane (horizontal axis) and as the length L_c along the *c*-direction (vertical axis). The colour code depicts the corresponding mass fraction of each D_{ab}, L_c combination. Comparing the 2D maps at low (5 min) and high (96 h) maturation times, a clear growth of the crystals along the *c*-axis is observed, either for cAp or Ap samples, along with a wide distribution of sizes; conversely, a limited growth and a narrow distribution is found in the orthogonal direction (*ab*-plane).

Average crystal sizes (and size distributions, σ) have been derived from the bivariate log-normal function of each sample, for both the hexagonal and the platy shapes. In the first case, (mass-based) values are given as $<D_{ab}>$, σ_{ab} and $<L_c>$, σ_c
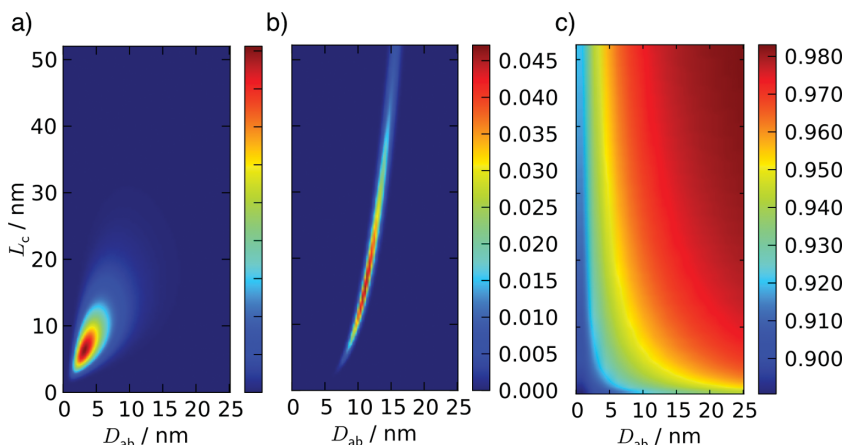
Figure 5. 2D maps, in the L_c and D_{ab} space, (L_c is the length along the *c*-axis, D_{ab} is the diameter of the circle of equivalent area in the *ab*-plane) of the bivariate log-normal size distribution of CDHA population in a) cAp 5 min and b) cAp 96 h samples; c) 2D map of the size-dependent site occupancy factor of the Ca2 atom (see inset of Figure 3) on increasing crystal size in the cAp 96 h sample.

(**Figure 6**a); in the latter case, the average crystal width (<W>) and thickness (<T>) in the *ab*-plane are shown in Figure 6b (σ_W, σ_T are available in Table SI.4, Supporting Information), the crystal length, <L_c>, being the same for the two morphologies. Upon maturation, crystals of progressively larger sizes along the two (or three, for platelets) growth directions are found; in cAp, crystals are systematically smaller and less anisotropic than in Ap, in agreement to what reported in the literature (as the effect of the carbonate substitution);[19] average aspect ratios (<L_c>/<D_{ab}>) are 2.0/2.2 and 2.4/2.8 in cAp and Ap samples, respectively.

Number-based size distributions, accessible at the end of the DFA process, have been used in the present study to calculate

the specific surface area of each Ap and cAp sample. Combining these values and the thermogravimetric estimates of the amount of citrate, the citrate surface density was evaluated as 1 molecule/(n nm)^2: in the investigated samples, n ranges between 1.6–2.0 (see Table SI.6, Supporting Information). Number- and mass-based averages (size and distribution) of all samples are synoptically collected in Tables SI.3 and SI.4 (Supporting Information).

An important structural feature of biomimetic Ca-deficient apatites relies on the Ca/P ratio which can strongly affect their dissolution properties.[20] Ca/P values were obtained for the investigated samples by Inductively Coupled Plasma Optical Emission Spectroscopy (ICP-OES);[10c] however, this kind of analysis provides a global indicator in which the likely different Ca/P ratios of the amorphous and the crystalline components within the same sample cannot be distinguished. DFA method allows the Ca/P ratio of the crystalline apatite to be estimated independently of the co-existing ACP fraction. These values have been obtained for Ap and cAp samples by refining the site occupancy factor (*sof*) of the two independent Ca atoms of the apatite structure (see inset of Figure 3). We also refined the *sof* of the hydroxyl O atom, whose amount may fluctuate as a function of the Ca deficiency and the crystal structure defectiveness,[21] and the isotropic Debye-Waller factor of all atoms. Refined Ca *sof*'s and Ca/P ratios derived there from for CDHA crystals only [Ca/P$_{(DFA-Cr)}$] are reported in **Table 1**. Values [Ca/P$_{(DFA-T)}$] taking the ACP fraction into account (Ca/P$_{ACP}$ = 1.71 ± 0.03) are also provided and seem to be fairly in agreement to the ICP-OES-determined Ca/P ratios.

Major deviations can be observed in the most mature Ap and cAp samples (96 h). Interestingly, more stoichiometric apatite crystals are "detected" by DFA upon maturation, likely due to self-healing processes occurring with time.[20] *Sof*'s in Table 1 refer to values from a size-independent model. Size-dependent *sof*'s have been refined only in the 96 h samples (see the 2D map of Ca2 in Figure 4c) which provided: in cAp sample, a fairly constant *sof* ≈ 0.992 (Ca1), values in the range 0.91/0.97 for Ca2 and 0.42/0.44 for O$_{OH}$, on increasing the crystal size (mainly along the *c*-axis, according to the size distribution map of Figure 2c); in Ap sample: *sof* ≈ 1.0 (Ca1), 0.92/0.95 (Ca2) and 0.5 (O$_{OH}$). Finally, reasonable values of the (size-independent) atomic Debye-Waller factors were obtained: the values (reported in Tables SI.5, Supporting Information) ranged from 0.9 to 1.5 (Å^2) for Ca, P and phosphate-O atoms, while larger parameters (in the 2.5/4.8 Å^2 range and decreasing at larger crystal sizes) were found for O$_{OH}$.

To complete the total scattering characterization of the investigated samples, we performed
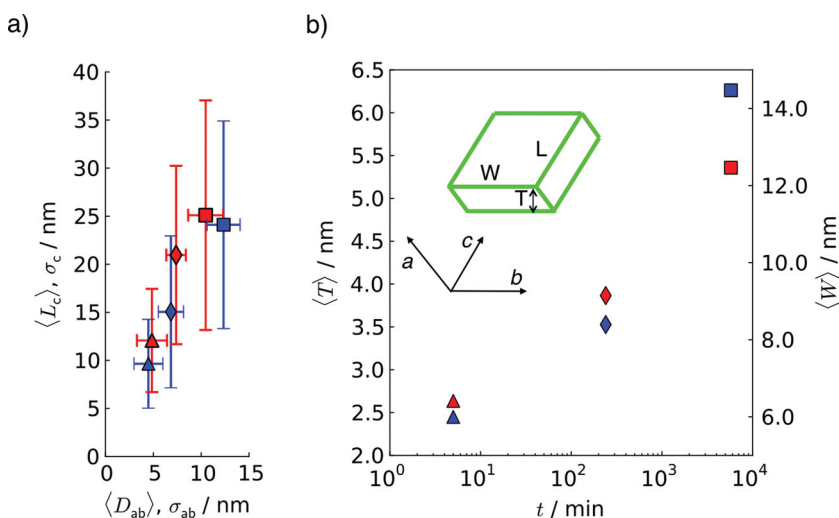

Figure 6. a) Average sizes of Ca-deficient hydroxyapatite crystals of hexagonal shape at growing maturation time: △5 min; ◇4 h; □96 h (red symbols refer to Ap samples, blue symbols to cAp samples). Values are given as crystal length (<L_c>, σ_c) and diameter of the circle of equivalent area (<D_{ab}>, σ_{ab}). In all samples a striking difference is found between the crystal size distribution along the *c*-axis and normal to it; b) average thickness (T) and width (W) of platy crystals (the crystal length L is the same as in a, see text for details). The inset shows the assignment of T, W, L to both crystal domains and nanoparticles.

Table 1. Site occupancy factor (*sof*) for Ca$_1$ (Wyckoff's *4f*), Ca$_2$ (Wyckoff's *6h*), and hydroxyl O atoms (Wyckoff's *6h*); Ca/P$_{(DFA-Cr)}$ ratios are derived by DFA for the crystalline apatite component and Ca/P$_{(DFA-T)}$ by adding to these values the ICP–OES-determined value for ACP (1.71±0.03), suitably weighted taking into account the corresponding weight fraction in each sample. Ca/P$_{(ICP-OES)}$ are the ICP–OES-determined Ca/P values (taken from the literature).[10c]

Sample[a]	Sof Ca$_1$	Sof Ca$_1$	Sof O$_{OH}$	Ca/P$_{(DFA-Cr)}$	Ca/P$_{(DFA-T)}$	Ca/P$_{(ICP-OES)}$
Ap 5 min	0.937	0.919	0.5	1.54	1.57	1.53 ± 2
Ap 4 h	0.979	0.892	0.5	1.54	1.56	1.51 ± 2
Ap 96 h	1.000	0.949	0.46	1.62	1.63	1.54 ± 2
cAp 5 min	0.946	0.914	0.5	1.54	1.57	1.60 ± 2
cAp 4 h	0.983	0.957	0.44	1.61	1.62	1.60 ± 2
cAp 96 h	0.993	0.971	0.43	1.63	1.64	1.58 ± 2

[a]Estimated standard deviation (e.s.d.) values of refined *sof* parameters fall near 10^{-4} and are highly unrealistic, being determined mainly by the extremely high synchrotron data counting rates under the assumption of processing data free of systematic errors. Similar concerns have been raised in conventional powder diffraction analyses (see Supporting Information). Therefore, the reported parameter values have been approximated to more sensible numbers.

the radial distribution function of the ACP (the instantaneously precipitated material) and of the cAp 96 h (the most mature one). The results are plotted as G(r) function in **Figure 7**. The first two peaks correspond to the nearest-neighbour P-O (1.5 Å), Ca-O (2.4 Å) and O-O (2.5 Å) inter-atomic distances, respectively (the assignment of additional peaks is depicted in Figure SI.4). For r < 5 Å, peaks indicate a similar local organization around each calcium ion in the two samples. Moreover, G(r) shows that the particle correlation length in ACP does not extend over 10 Å. This value well matches the (theoretically calculated) radius of Posner's cluster[22] (the purported common building unit of ACP and apatite), as well as the size of experimentally detected calcium
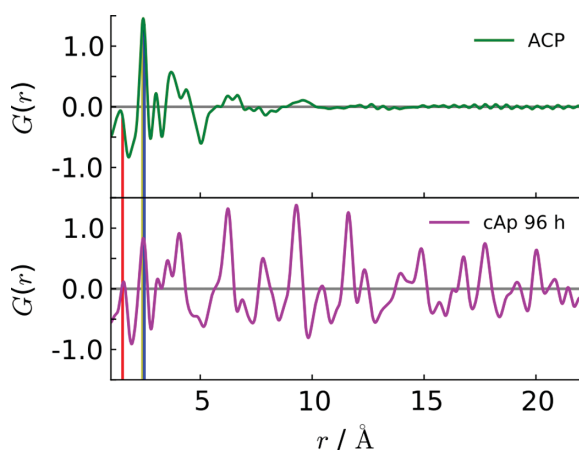

Figure 7. Reduced G(r) function providing a plot of atomic number density *vs.* atomic separations in ACP (top) and cAp 96 h (bottom) samples; positive and negative peaks correspond to density higher or lower than the average one, respectively. The first two peaks correspond to the nearest-neighbour P-O (1.5 Å, red vertical bar), Ca-O (2.4 Å, grey vertical bar) and O-O (2.5 Å, blue vertical bar) interatomic distances, respectively. G(r) shows that the ACP correlation length does not extend over 10 Å and, at low r values (below 5 Å), peaks indicate a similar local organization around each calcium ion in the two samples.

phosphate clusters (by dynamic light scattering)[23] and stable pre-nucleation clusters (high-resolution cryo-transmission electron microscopy)[7] in simulated body fluids, and, to some extent, also the slightly polydispersed ACP NP thicknesses of 1.1±0.5 nm measured by AFM in the present study and described in section 3. Very recently, the nano-sized entities named pre-nucleation clusters elsewhere,[7] were identified by the same group of authors as were the soluble calcium triphosphate complexes which aggregate in solution and, after taking up Ca^{2+} ions, precipitate as ACP, which is a fractal of Ca$_2$(HPO$_4$)$_3^{2-}$ clusters.[24]

In the present study, concerning the role of the pre-nucleation (or Posner) clusters or of the purported soluble polynuclear complexes, our observations on the structural and morphological evolution of apatite (discussed in Section 4) seem to be in favour of a NC growth from a solid precursor in which smaller pre-organized entities progressively grow within the ACP NPs, but we cannot confirm or exclude that these clusters are ion association complexes.

3. AFM Characterization of Bio-Inspired Apatite Nanoparticles

The size and morphology evolution of Ap and cAp NPs was also assessed by ex situ AFM measurements. The sub-nanometer vertical resolution (better than 0.1 nm) of the AFM images was used, in particular, to obtain reliable values of the NPs thickness. **Figure 8** shows selected AFM images of ACP, Ap and cAp (maturation time: 96 h) deposited on freshly cleaved mica surfaces. The z-section of the ACP particles shown in the inset clearly indicate that they are platelets, the average sample thickness of 1.1±0.5 nm being much smaller than both its average length and width. The total scattering analysis presented in section 2.2 on samples precipitated under the same conditions revealed the amorphous nature of these particles. That ACP, before and after AFM investigations, remained unchanged was confirmed by X-ray diffraction and Raman spectroscopy (not shown here).

The formation of platy amorphous calcium phosphate NPs is a fairly unusual finding. Other authors have recently observed,[25] by in situ AFM, ACP (or poorly crystalline apatite) platelets, 2.3 nm thick, forming on the surface of calcite crystals through a surface-induced mechanism initiated by the aggregation of clusters and leading to the nucleation and growth of ACP/apatite particles. Very interestingly, the process
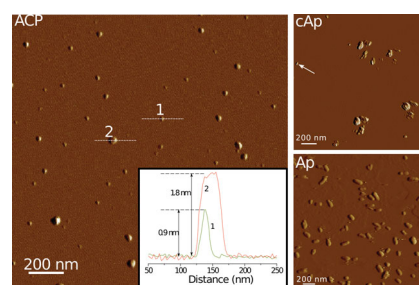

Figure 8. AFM images revealing the platy morphology of NPs for ACP, Ap 96 h and cAp 96 h samples. The inset shows the z-section of ACP NPs 1 and 2.

ADVANCED
FUNCTIONAL
MATERIALS
www.afm-journal.de

Materials
Views
www.MaterialsViews.com

FULL PAPER

was observed in the presence of citrate which, in low concentration, increased the mineral nucleation rate. Analogously to the observations reported in, the ACP platelets observed in the present study might be explained by the action of a template surface favoring the oriented aggregation of calcium phosphate clusters. López-Macipe et al.[10a] already proposed that calcium phosphate heterogeneously nucleates on the surface of sodium citrate crystals grown in the early stages. They suggested that the formation of the template was crucial to obtain apatite particles with nanosized-dimensions. In the present study, submicrometer-sized $Na_3(cit) \cdot 2H_2O$ and $Na_3(cit) \cdot 5.5H_2O$ crystals were also detected by X-ray diffraction at the earliest stages (as shown in Figure SI.6), and disappeared very rapidly. Thus, we suggest that the ACP platelets originate by the oriented aggregation of clusters adsorbed on the surface of sodium citrate crystals, which later dissolve by sudden pH changes (vide infra). Worthy of note, the formation of amorphous ribbons in the absence of citrate was reported by Habraken et al.;[24] in this case ACP partially transforms into a transient octacalcium phosphate, which was never detected in our samples; however, the formation of octacalcium phosphate in the absence of citrate was confirmed in our blank experiments (see Experimental Section and Figure SI.7, Supporting Information).

Table 2 summarizes the dimensions of the NPs as measured by AFM. In all samples, the nanoparticles are platelets increasing their thickness upon maturation time. ACP appears as isometric NPs (in the imaging plane) whereas Ap and cAp are clearly elongated. Their morphology evolution showed opposite trends: Ap NPs increased their width and length; cAp NPs slightly thickened while the other two dimensions progressively reduced. A detailed discussion of these findings is presented in section 4.

4. Discussion

In this section a tentative interpretation of the structural and morphological evolution of the citrate-controlled calcium phosphate NPs is discussed by cross-coupling the Total Scattering (DFA and G(r)) and AFM results. AFM analysis shows that tiny platelets form at the earliest stages of precipitation (Figure 8a,

ACP), amorphous in nature, the correlation length [ca. 1 nm, as measured by the G(r) function] of which matches the ACP NP thicknesses of 1.1±0.5 nm measured by AFM. On increasing the maturation time, Ap and cAp appear as thicker but still platy NPs (Figure 8). DFA indicates, after 5 min, the presence of apatite nanocrystals coexisting with a non-negligible amount of ACP (ca. 18 wt%); the majority of crystals (more than 90 wt% of the crystal fraction) are tiny, platy shaped domains ca. 2.5 nm thick, 6.0 nm wide and 9.6 nm long (Figure 6a,b). Upon maturation, larger crystals of preferential hexagonal shape (up to 70 wt%) develop while the content of ACP progressively decreases (below 10 wt%). Ap and cAp samples mainly differ in the systematically smaller sizes and the lower aspect ratios of nanocrystals in cAp.

Interestingly, all samples show a broad distribution of crystal lengths along the c-axis while they are narrowly distributed in the ab-plane, regardless of the chemical environment and precipitation time. Moreover, the estimated citrate surface density of 1 molecule/$(n$ nm$)^2$, n ranging between 1.6–2.0, is very close to the value previously reported for avian and bovine bone.[9a] Both findings, the narrow crystals size distribution normal to the {10–10} facets and their citrate coverage, agree well with the mechanism, hypothesized in bone mineralization, of adsorbed citrate stabilizing the apatite crystals thickness.[9a,b] Nonetheless, they do not explain the preferential platy shape of crystals found at low maturation times.

To this aim, we compared in **Figure 9** the average thickness (T_{DFA}), width (W_{DFA}) and length (L_{DFA}) of CDHA *crystal domains* provided by DFA, and those determined by AFM on whole *single NPs* (T_{AFM}, W_{AFM}, L_{AFM}), disregarding their amorphous or crystalline nature. In this comparison, thickness (T), width (W) and length (L) are assigned to the platelets (either crystal domains or NPs), as in Figure 6b (T < W < L,) which shows, additionally, the mutual orientation of crystallographic axes and NPs surface. T_{DFA} and W_{DFA} were obtained by suitably weighting the values from the hexagonal and platy morphologies, according to the mass fractions reported in Figure 4.

Importantly, crystal thickness systematically fits that of NPs ($T_{DFA} \approx T_{AFM}$) until 4 h maturation (Figure 9a), while width and length are systematically smaller in crystals than in NPs ($W_{DFA} < W_{AFM}$ and $L_{DFA} < L_{AFM}$, Figure 9b,c). Therefore, at low and medium maturation time, the NPs *must be* single crystal domains along T_{AFM} and multiple crystal domains along W_{AFM} and L_{AFM}. The coincidence of T_{DFA} and T_{AFM} (the shortest sizes), moreover, indicates that crystals are oriented with their (01$\bar{1}$0) plane parallel to the NP surface imaged by AFM (compare Figure 2b and Figure 6b). This enabled us to infer the anisotropic growth along the crystallographic a- and b-axes (breaking the hexagonal symmetry and giving rise to platy crystals). Indeed, the growth is expected to stop in one direction because of the finite thickness of the parent amorphous platelets (T_{AFM}) and the further binding of citrate on the surface, but to freely continue in the other directions within each NP, therefore increasing W_{DFA} and L_{DFA}, as later substantiated.

After 96 h, crystals and NPs no longer show the same thickness. Time-dependent pH variations (Figure SI.5, Supporting Information) and the tendency toward dissolution of the smallest crystals (which show, in addition, a lower Ca/P ratio, see Figure 5c) might favor particle aggregation/re-crystallization
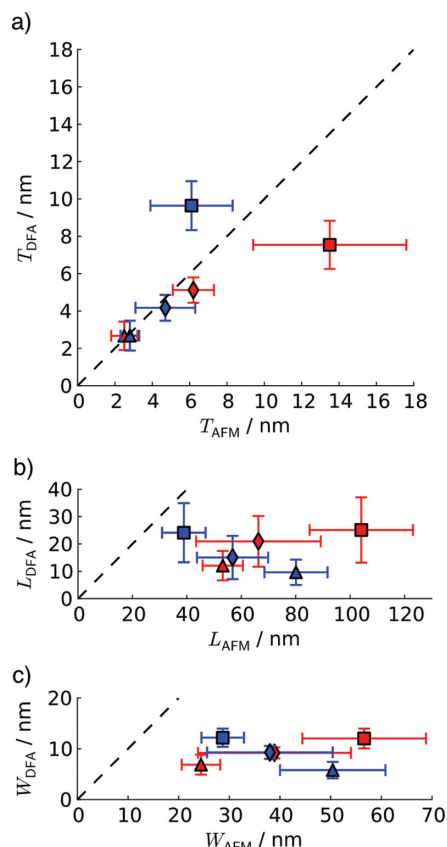
Table 2. (Number-based) average linear dimensions (nm) and their variances for nanoparticles imaged by AFM. Thickness (T_{AFM}), Width (W_{AFM}) and Length (L_{AFM}) are assigned according to Figure 6b

Sample[a]	< L_{AFM} >	< W_{AFM} >	< T_{AFM} >
ACP	35.5 ± 6.9	34.7 ± 6.5	1.1 ± 0.5
Ap 5 min	53.2 ± 7.4	24.4 ± 3.8	2.5 ± 0.7
Ap 4 h	66.3 ± 22.9	38.9 ± 15.1	6.2 ± 1.1
Ap 96 h	104.1 ± 19.0	56.6 ± 12.2	13.5 ± 4.1
cAp 5 min	80.1 ± 11.6	50.4 ± 10.4	2.8 ± 0.5
cAp 4 h	56.8 ± 13.1	38.0 ± 12.4	4.7 ± 1.6
cAp 96 h	38.9 ± 8.0	28.7 ± 4.2	6.1 ± 2.2

[a]The AFM averages are compared in Figure 9 to the mass-based values (instead of the number-based ones) derived by DFA. This choice relies on the fact that the mass-based DFA-values are more representative of the whole sample, which is therefore more safely compared to finest particles analyzed by AFM.

www.MaterialsViews.com

ADVANCED
FUNCTIONAL
MATERIALS
www.afm-journal.de

FULL PAPER

Figure 9. a) Average thickness of crystal domains provided by Debye function (DFA) method (T_{DFA}) vs the average thickness of NPs (regardless of their crystalline or amorphous nature) provided by AFM (T_{AFM}); b) average length of crystal domains (L_{DFA}) vs the average length of NPs (L_{AFM}) and c) average width of crystal domains (W_{DFA}) vs the average width of NPs (W_{AFM}). The vertical and horizontal bars depict the DFA- and AFM-derived distributions about each average. The broken line is a guide to the eye to easily identify samples having very similar DFA- and AFM-derived dimensions.

sample volume, while AFM analyzes only the finest fraction. Therefore, in the cAp 96 h case, the single NPs might be more selectively made of platy crystals, whose thickness well fits that of NPs (ca. 6 nm, compare Figure 6b and Table 2) and accounting for ca. 30 wt% of the total crystal fraction (Table SI.2, Supporting Information). The remaining larger hexagonal crystals are expected to fall into the bigger aggregates. If the same assumption is taken for the youngest samples of Figure 6, results do not change significantly since platy crystals are nearly ubiquitous in the 5 min samples and the major fraction in the 4 h samples.

On the basis of the foregoing results, we propose a plausible mechanism, depicted in **Figure 10**, for the formation of apatite platelets. In the model system here investigated citrate ions seem to play multiple roles. The sodium citrate crystals detected at the earliest stages[26] are thought to act as a template surface which, through adsorption of ionic species (Ca^{2+}, HPO_4^{2-} and OH^-, neglecting the minor ones), might trigger the heterogeneous nucleation process through surface formation of "clusters" that, laterally aggregating, form ACP particles with unusual platy morphology;[25] alternatively, the template surface might adsorb calcium phosphate clusters already formed in solution. The drop of pH and the temperature changes in the initial stages (Figure SI.5, Supporting Information) produce partial dissolution of the template leading to the formation of $Hcit^{2-}/cit^{3-}$, which partially bind to the ACP platelets. The presence of adsorbed citrate on the surface slows down the plate thickening by inhibiting further ion adsorption and NP aggregation. Apatite crystals start to grow from multiple nuclei *within* each ACP platelet. The hexagonal crystal symmetry enables independent growth of each nucleus along the *c*-axis and in the orthogonal *ab*-plane (isotropically along the *a*- and *b*-axes) (stage 1) until the NP platelet surface is reached. At this point (stage 2) citrate ions, strongly bound to surface Ca^{2+} ions on the free (10–10) crystal facet, stop any further growth in this direction, which anyway continues in the other two (in the presence of as yet untransformed amorphous material) (stage 3) until separately nucleated crystal domains touch each other. Platy crystals of the same thickness as ACP platelets are thus formed at low maturation times. After 4 h (stage 4), this mechanism
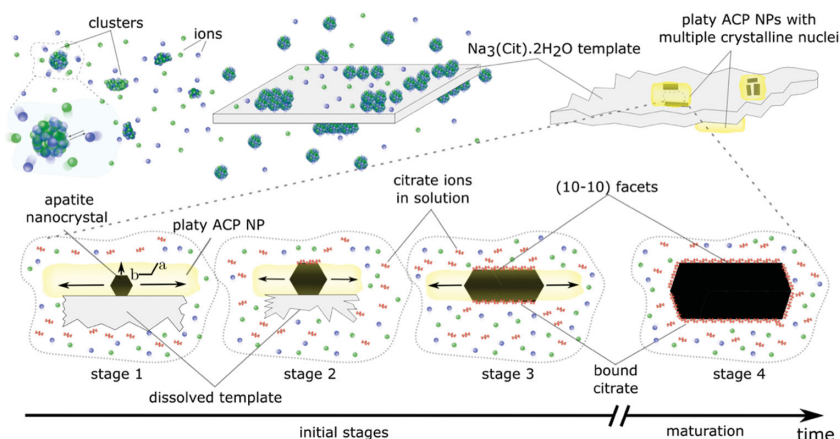
phenomena.[20] Therefore, new size and shape distributions of crystals and NPs are likely to form. These processes are witnessed by the change towards a preferential hexagonal shape of crystals (according to the DFA findings) and the different way Ap and cAp NPs changed their size and shape (according to the AFM study). Indeed, Ap NPs grew along all three directions (T_{AFM}, W_{AFM} and L_{AFM}) with multiple crystal domains appearing even along their thickness. In contrast, cAp NPs slightly thickened while they progressively shrank in W_{AFM} and L_{AFM} (Figure 9b,c), T_{DFA} being 1.5 times larger than T_{AFM} (Figure 9a), a rather difficult to interpret conundrum. A tentative explanation is hereafter proposed and takes into account that, in DFA, crystal sizes are representative of the entire irradiated

Figure 10. Schematics of the mechanism forming apatite platelets during the ACP-to-crystal transformation. A time scale of minutes applies to the initial stages and hours to the maturation process.

is still active in controlling the average crystal thickness. However, the hexagonal crystal morphology begins to appear (or, in other words, the average crystal anisotropy in the *ab*-plane starts to decrease), concomitantly with dissolution, aggregation, recrystallization phenomena and becomes dominant after 96 h, forming larger (more stoichiometric) apatite crystals.

5. Conclusions

We presented a total scattering method which offers a multivalent approach to quantitatively investigate many aspects of interest (structure, stoichiometry, size and morphology) in biomimetic apatites within a unique, organic framework. Additional advantages rely on the statistical significance of the DFA-derived parameters, which are averaged over millions of particles (of all kinds present in the sample), if compared to the few hundreds (possibly selected by preparation) analyzed by any kind of microscopy. The amorphous-to-crystalline transformation process here described and the appealing mechanism inducing the platy morphology in bio-inspired apatite nanocrystals show, for the first time, the role of citrate in driving the formation of platy apatite NCs similar to those formed in bone under the control of acidic non-collagenous proteins, collagen fibrils and, likely, citrate ions. A similar mechanism might be at work in bone mineralization, where citrate ions might play a broader role than has been depicted to date. Finally, the quantitative picture of the structural, compositional and morphological evolution of citrate-controlled apatite nanoparticles, here presented, can be of great relevance in tuning the properties of this important class of biomaterials for advanced applications.

6. Experimental Section

Synthesis of Ap and cAp Samples: Calcium chloride dihydrate ($CaCl_2.2H_2O$, Bioxtra, ≥99,0% pure), sodium citrate tribasic dihydrate ($Na_3(Cit).2H_2O$ where Cit = citrate = $C_6H_5O_7$, ACS reagent, ≥99,0% pure), sodium phosphate dibasic (Na_2HPO_4, ACS reagent, ≥99,0% pure) and sodium carbonate monohydrate ($Na_2CO_3.H_2O$, ACS reagent, 99.5% pure) were supplied by Sigma-Aldrich. All the solutions were prepared with ultrapure water (0.22 µS, 25 °C, MilliQ, Millipore). The nanocrystals were obtained by a batch heating method described elsewhere.[10c] Briefly, two solutions (1:1 v/v, 200 mL total) of (i) 0.1 M $CaCl_2$ + 0.4 M $Na_3(Cit)$ and (ii) 0.12 M Na_2HPO_4, + x mM Na_2CO_3 (x = 0 or 100) were mixed at 4 °C. The pH of the mixture was adjusted with HCl to 8.5. The mixture was then introduced in a 250 mL round-bottom flask, sealed with a glass stopper and immersed in a water bath at 80 °C. The precipitates were then matured in the mother solution for 5 min, 4 h, and 96 h at 80 °C. An additional experiment with x = 100 mM was carried out by collecting the powder just after immersing the metastable solution in the flask at 80 °C (time 0). This powder was analyzed by X-ray powder diffraction (see ACP trace in Figure 1b) and Raman spectroscopy (inset of Figure SI.6). Its chemical formula, obtained by TGA and ICP-OES, is $Na_{1.8}Ca_{8.1}(PO_4)_{4.75}(CO_3)_{1.35}(OH)(H_2O)_4$.

A hot-line pH probe (Sentron, Netherlands) immersed in the flask allowed in situ measurements of the pH and the Temperature continuously during the precipitation process (Figure SI.5, Supporting Information). After the precipitation, the particles were repeatedly washed with ultrapure water (MilliQ, Millipore) by centrifugation, freeze-dried (LyoQuest, Telstar, Spain) and stored at 4 °C for further characterization. Powders obtained without Na_2CO_3 are referred to as Ap, whereas those obtained in the presence of 100 mM Na_2CO_3 are referred to as cAp.

Finally, two samples were synthesized using the same batch heating method in the absence of citrate, matured for 5 min and 4 h, respectively. Laboratory X-ray powder diffraction patterns revealed a totally different pathway, compared to the case in which citrate ions are used: at 5 min, a sample made of nanosized octacalcium phosphate was obtained; at 4 h, nanosized apatite is found as the major phase together with a minor presence of octacalcium phosphate. The two diffraction pattern were modelled using the Rietveld method implemented in the program TOPAS-R; the best fits are shown in Figure SI.7, Supporting Information.

Synchrotron X-ray Total Scattering Measurements: Powder samples were loaded in glass capillaries of 0.5 mm diameter and measured at the X04SA-MS Beamline of the Swiss Light Source of the Paul Scherrer Institut in Villigen, CH. The beam energy was set at 15 keV and the operational wavelength (λ = 0.82669 Å) precisely determined by collecting, under the same experimental conditions, a silicon powder standard [NIST 640c, a_0 = 0.54311946(92) nm at 22.5 °C]. Data were collected in the 2–130° 2θ range with the aid of the position sensitive single-photon counting MYTHEN II detector.[27] Independent He/air and capillary scattering curves, as well as empty and sample-loaded capillary transmission coefficients, were also measured and used for data subtraction of all extra-sample scattering effects and absorption correction.[28] Inelastic (Compton) scattering (strongly visible in all patterns at the beam energy of 15 keV) was calculated and directly added to the Debye pattern model. Cell parameters for each sample were derived by the conventional Rietveld method implemented in the program TOPAS-R.[29] We used symmetrized spherical harmonics to cope, phenomenologically, with anisotropic peak broadening effects due to the anisotropic crystal shape. To evaluate the match between the experimental and DFA pattern model, the statistical agreement index R_{wp} was used for each dataset; the Goodness of Fit (GoF) statistical descriptor, measuring the goodness of the model with respect to the experimental data, is also provided: GoF = 1 is the expected value for a perfect model; values in the range 5–6 are common for synchrotron data with high counting statistics.[30]

Radial Distribution Function (RDF): Total Scattering data can also be analyzed in real, rather than in reciprocal space, using the so-called Radial or Pair Distribution Function technique, which gives one-dimensional plots of sine-Fourier-transformed scattering data. This function provides a plot of atomic number density *vs.* atomic separations present in the sample. We computed the RDF [in the form of reduced G(r)] for the most crystalline sample of the cAp series (96 h) and for the amorphous ACP material. In the reduced G(r) function, positive and negative peaks correspond to density higher or lower than the average one, respectively.

Atomic Force Microscopy: The size of the NPs was measured by Atomic Force Microscopy (AFM) that is a powerful non-invasive tool to measure the size and height of samples with nanometer and even sub-nanometer resolution.[31] For these experiments, the freeze-dried powdered samples were dispersed in ultrapure water and then the suspension was filtered (0.22 µm, Millipore) in order to remove the bigger aggregates. A drop of the latter slurry was deposited on the atomically flat surface of a freshly cleaved mica substrate. The mica surface was subsequently dried by evaporation overnight at room temperature in a vacuum desiccator before the AFM analysis. The images were collected with a Nanoscope IIID microscope (Digital Instruments, Veeco, Santa Barbara, USA) in tapping mode by scanning the surface in air with silicon probes (NCHV, spring constant of 42 N m⁻¹ and resonant frequency of 320 kHz, Veeco Probes, Santa Barbara, USA). Thickness, width and length (see inset of Figure 4d) were measured on more than 30 single (non-aggregated) nanoparticles for each sample. The vertical and lateral resolutions were better than 0.1 nm and 10 nm, respectively.

Elemental and Thermal Analyses of the ACP sample: Performed following the protocol described elsewhere.[10c]

Supporting Information

Supporting Information is available from the Wiley Online Library or from the author.

Materials
Views

www.MaterialsViews.com

ADVANCED
FUNCTIONAL
MATERIALS

www.afm-journal.de

FULL PAPER

[1] a) F. Nudelman, N. A. J. M. Sommerdijk, *Angew. Chem. Int. Ed.* **2012**, *51*, 6582; b) R. Z. LeGeros, *Chem. Rev.* **2008**, *108*, 4742; c) H. P. Rim, K. H. Min, H. J. Lee, S. Y. Jeong, S. C. Lee, *Angew. Chem. Int. Ed.* **2011**, *50*, 8853; d) J. Gómez-Morales, M. Iafisco, J. M. Delgado-López, S. Sarda, C. Drouet, *Progr. Cryst. Growth* **2013**, *59*, 1–56.

[2] a) J. Mahamid, A. Sharir, L. L. Addadi, S. Weiner, *Proc. Natl. Acad. Sci. USA* **2008**, *105*, 12748; b) J. Mahamid, B. Aichmayer, E. Shimoni, C. Li, S. Siegel, O. Paris, P. Fratzl, S. Weiner, L. Addadi, *Proc. Natl. Acad. Sci. U. S. A.* **2010**, *107*, 6316; c) F. Nudelman, K. Pieterse, A. George, P. H. H. Bomans, H. Friedrich, L. J. Brylka, P. A. J. Hilbers, G. de With, N. A. J. M. Sommerdijk, *Nat. Mater.* **2010**, *9*, 1004; d) E. Beniash, *WIREs Nanomed. Nanobiotechnol.* **2011**, *3*, 47.

[3] a) S. J. Eppell, W. Tong, J. L. Katz, L. Kuhn, M. J. Glimcher, *J. Orthop. Res.* **2011**, *19*, 1027; b) P. Fratzl, H. S. Gupta, E. P. Paschalis, P. Roschger, *J. Mater. Chem.* **2004**, *14*, 2115.

[4] a) M. I. Kay, R. A. Young, A. S. Posner, *Nature* **1964**, *204*, 1050; b) J. C. Elliot, P. E. Mackie, R. A. Young, *Science* **1973**, *180*, 1055; c) Th. Leventouri, *Biomaterials* **2006**, *27*, 3339.

[5] a) N. J. Crane, V. Popescu, M. D. Morris, P. Steenhuis, M. A. Ignelzi Jr., *Bone* **2006**, *39*, 434; b) S. Weiner, *Bone* **2006**, *39*, 431.

[6] Y. Politi, T. Arad, E. Klein, S. Weiner, L. Addadi, *Science* **2004**, *306*, 1161.

[7] A. Dey, P. H. H. Bomans, F. A. Müller, J. Will, P. M. Frederik, G. de With, N. A. J. M. Sommerdijk, *Nat. Mater.* **2010**, *9*, 1010.

[8] S. V. Dorozhkin, *Acta Biomater.* **2010**, *6*, 715.

[9] a) Y.-Y. Hu, A. Rawal, K. Schmidt-Rohr, *Proc. Natl. Acad. Sci. U. S. A.* **2010**, *107*, 22425; b) B. Xie, G. H. Nancollas, *Proc. Natl. Acad. Sci. U. S. A.* **2010**, *107*, 22369.

[10] a) A. López-Macipe, J. Gómez-Morales, R. Rodríguez-Clemente, *Adv. Mater.* **1998**, *10*, 49; b) Y.-Y. Hu, A. Rawal, T. Prozorov, M. Akinc, S. K. Mallapragada, K. Schmidt-Rohr, *Chem. Mater.* **2011**, *23*, 2481; c) J. M. Delgado-López, M. Iafisco, I. Rodríguez, M. Prat, J. Gómez-Morales, *Acta Biomater.* **2012**, *8*, 3491.

[11] a) T. Egami, S. J. L. Billinge, in *Underneath the Bragg Peaks: Structural Analysis of Complex Materials*, Pergamon Press, Oxford, UK **2003**; b) P. Debye, *Ann. Phys.* **1915**, *46*, 809; c) A. Cervellino, C. Giannini, A. Guagliardi, *J. Appl. Cryst.* **2010**, *43*, 1543; d) G. Cernuto, S. Galli, F. Trudu, G. M. Colonna, N. Masciocchi, A. Cervellino, A. Guagliardi, *Angew. Chem. Int. Ed.* **2011**, *50*, 10828.

[12] Energy calculations support the preference of citrate binding to $\{01\bar{1}0\}$ versus $\{0001\}$ facets} versus $\{0001\}$ facets: M. R. T. Filgueiras, D. Mkhonto, N. H. Leeuw, *J. Cryst. Growth.* **2006**, *294*, 60.

[13] Standard powder diffraction methods such as the Rietveld approach for structural analysis and the Scherrer equation for crystal size domain estimation, rely on Bragg scattering only.

[14] a) R. Z. LeGeros, O. R. Trautz, J. P. LeGeros, E. Klein, W. P. Sirra, *Science* **1967**, *155*, 1409; b) S. V. Dorozhkin, M. Epple, *Angew. Chem. Int. Ed.* **2002**, *41*, 3130.

[15] A. Cervellino, C. Giannini, A. Guagliardi, *J. Comput, Chem.* **2006**, *27*, 995.

[16] Th. Leventouri, C. E. Bunaciu, V. Perdikatsis, *Biomaterials* **2003**, *24*, 4205.

[17] a) P. D. Sampson, A. F. Siegel, *J. Am. Stat. Assoc.* **1985**, *80*, 910; b) G. Cernuto, N. Masciocchi, A. Cervellino, G. M. Colonna, A. Guagliardi, *J. Am. Chem. Soc.* **2011**, *133*, 3114.

[18] a) A. Guagliardi, A. Cedola, C. Giannini, M. Ladina, A. Cervellino, A. Sorrentino, S. Lagomarsino, R. Cancedda, M. Mastrogiacomo, *Biomaterials* **2010**, *31*, 8289; b) G. Campi, A. Ricci, A. Guagliardi, C. Giannini, S. Lagomarsino, R. Cancedda, M. Mastrogiacomo, A. Cedola, *Acta Biomater.* **2012**, *8*, 3411.

[19] R. Z. LeGeros, O. R. Trautz, J. P. LeGeros, E. Klein, W. P. Sirra, *Science* **1967**, *155*, 1409.

[20] L. Wang, G. H. Nancollas, *Chem. Rev.* **2008**, *108*, 4628.

[21] G. Cho, Y. Wu, J. L. Ackerman, *Science* **2003**, *300*, 1123.

[22] A. A. Posner, F. Betts, *Bone Min. Str.* **1975**, *8*, 273.

[23] K. Onuma, A. Ito, *Chem. Mater.* **1998**, *10*, 3346.

[24] W. J. E. M. Habraken, J. Tao, L. J. Brylka, H. Friedrich, L. Bertinetti, A. S. Schenk, A. Verch, V. Dmitrovic, P. H. H. Bomans, P. M. Frederik, J. Laven, P. van der Schoot, B. Aichmayer, G. de With, J. J. DeYoreo, *Nature Commun.* **2013**, *4*, 1.

[25] L. Wang, E. Ruiz-Agudo, C. V. Putnis, M. Menneken, A. Putnis, *Environ. Sci. Technol.* **2012**, *46*, 834.

[26] According to the data proposed by Gao et al. (J. Gao, C. Xie, Y. Wang, Z. Xu, H. Hao *Crys. Res. Tech.* **2012**, *47*, 397) the actual concentration values of citrate are well below the supersaturation level at any temperature in the 0–100 °C range; however the occurrence of pH changes and of several complexation equilibria when Ca^{2+} ions are present forces the precipitation of a small amount of tiny sodium citrate crystals, observed also in blank experiments performed by adding $CaCl_2$ uniquely to ca. 0.4 M solution of sodium citrate.

[27] A. Bergamaschi, A. Cervellino, R. Dinapoli, F. Gozzo, B. Henrich, I. Johnson, P. Kraft, A. Mozzanica, B. Schimtt, X. Shi, *J. Synchrotron Rad.* **2010**, *17*, 653.

[28] A. Cervellino, R. Frison, G. Cernuto, A. Guagliardi, in *Crystallography for Health and Biosciences* (Eds. N. Masciocchi, A. Guagliardi), Insubria Univ. Press, Varese, Italy **2012**, p. 177.

[29] TOPAS-R (Bruker AXS, V.3.0, Karlsruhe, Germany).

[30] L. B. Mac Cusker, R. B. Von Dreele, D. E. Cox, D. Louër, P. Scardi, *J. Appl. Cryst.* **1999**, *32*, 36.

[31] Y. Gan, *Surf. Sci. Reports* **2009**, *64*, 99–121.